Highly-sensitive cell concentration detection by resonant optical tunneling effect

Aoqun Jian[1,2], Lu Zou[1,2], Gang Bai[1,2], Qianqian Duan[1,2], Yixia Zhang[1,2], Xuming Zhang[3,*], Shengbo Sang[1,2,*],

[1]MicroNano System Research Center, Key Lab of Advanced Transducers and Intelligent Control System of the Ministry of Education & College of Information and Computer, Taiyuan University of Technology, Jinzhong 030600, China
[2]Key Laboratory of Advanced Transducers and Intelligent Control System, Shanxi Province and Ministry of Education, Taiyuan 030024, China
[3]Department of Applied Physics, Hong Kong Polytechnic University, Hung Hom, Kowloon, Hong Kong, China
*Address correspondence to: apzhang@polyu.edu.hk (Xuming Zhang); sunboa-sang@tyut.edu.cn (Shengbo Sang)

Abstract

This paper presents an original design of volume refractive index (RI) sensor for cell concentration detection based on the unique resonant optical tunneling effect (ROTE). It is accomplished by introducing the solution sample into the ROTE resonant cavity, whose reflection spectrum presents a large shift of its sharp resonant dip in response to the tiny change of the solution RI. Performance calibration using the polystyrene (PS) particle solutions has shown the sensitivity of 19,000 nm/RIU and the total Q factor of 4,000. Here the top saturation method is adopted to narrow the spectral width of dip and to enhance the total Q factor by about 7 times. Experiments with hepatoma cells have obtained the sensitivity as high as 3.15 nm/(amol/ml) and the detection limit of 4×10^4 cells/ml. Compared with the reported optical cell sensors, this work is original due to the first use of the ROTE mechanism and is superior in the device performance. For instance, it enhances the sensitivity by about 40 times and the figure of merit by about 20 times as compared to the state of the art. These makes it highly potential for biomedical applications such as drug discovery, cell research and medical diagnoses.

Keywords: resonant optical tunneling effect, optical biosensor, cell concentration, figure of merit

1. Introduction

Cell concentration (number of cells/ml) is considered to be a key indicator to reflect a series of cell processes, such as viral infection (Peltola et al., 2006; Urszula et al., 2014; Vaisocherová et al., 2006), abnormal hematopoiesis (Jaitin et al., 2015), drug reactions (Fletcher et al., 2014), and autoimmune disease (Wallace et al., 2015). Usually, refractive index (RI) measurements are widely utilized to quantitatively analyze extremely small variations in the chemical components of a solution. For example, 10^{-9} RIU is equivalent to 1 femto-mol/L of salt in water. Recently, the RI measurement rises up as a real-time and label-free method to detect cell concentration at high resolution (Guo et al., 2014).

Nowadays, most of the sensing mechanisms/structures of the RI sensors are based on near-field optics, such as optical fiber Bragg grating (FBG) (Sun et al., 2017), long period fiber grating (LPG) (He et al., 2011; Rindorf et al., 2008), photonic crystal/photonic crystal fiber (PCF) (Hoo et al., 2009; Wu et al., 2009), and whisper gallery mode (WGM) (Luo et al., 2014; Scholten et al., 2014; Vollmer et al., 2002; Zhang et al., 2016; Zhi et al., 2017). Evanescent waves near the two-media interface are exploited for these detection methods. The strong confinement of the evanescent waves near the interface favors the strong light-analyte interaction. However, the intensity of evanescent wave decays exponentially when it goes away from the interface, which inevitably limits spatial interaction depth to the subwavelength range. These sensors cannot be used to effectively measure the entire biological sample with the size larger than the wavelength (e.g. eukaryotic cell, 10–100 μm) or the samples/particles naturally suspended in the solution. However, in the case of volume RI sensing, lightwaves completely propagate through the solution containing the targeted analyte and interact with every particle in the shaft, which is particularly useful for detecting the samples with ultralow concentration. Volume RI sensing can be realized by some classical methods/schemes, e.g., Febry-Pérot etalon. However, the complex fabrication process of a highly reflective mirror with tiny absorption prevents it from comprehensive commercial application (Cole et al., 2013; Cole et al.,

2016).

Since the first demonstration by Hayashi's group (Hayashi et al., 1999), the resonant optical tunneling effect (ROTE) has shown its uniqueness in bridging the wave optics and the quantum physics, and has found great potential in both theoretical studies and practical applications as photonic devices (Jian et al., 2013; Yamamoto et al., 2004). This study will present the first experimental demonstration of an RI sensor based on the ROTE. It overcomes the spatial limitation of the evanescent field to achieve high sensitivity detection of the whole cells. With simple fabrication, the sensor successfully detects hepatoma cell concentrations with a resolution of 4×10^4 cells/ml, and its figure of merit (FOM) value is one order higher than the other cutting-edge optical methods (Guo et al., 2014; Liu et al., 2014).

2. Concept & sensor design

The ROTE originates from a relatively simple phenomenon, the optical tunneling effect (a.k.a., frustrated total internal reflection, FTIR). When the incident angle θ is larger than the critical angle of the interface between high-low RI media, some of the evanescent light can pass through the total reflection interface to form the tunneled light, if the low-RI layer is thin enough. The ROTE briefly refers to the resonance effect of such tunneled light in a well-designed resonator. Its structure consists of five layers with a high-low-high-low-high distribution of RI, which are named in turn as: *input layer*, *first tunneling gap*, *central slab*, *second tunneling gap*, and *output layer* along the light propagating direction, as shown in Fig. 1a.

By using the finite difference time domain (FDTD) method, the electric field distributions of the ROTE structure at the resonant wavelength are illustrated in Fig. 1b (S-polarized light) and Fig. 1c (P-polarized light). It can be seen that for both polarization states, the electric field tends to decrease in the first tunneling gap, then forms locally enhanced mode in the central slab, like a standing wave, and finally decays in the second tunneling gap. These two graphs show that the incident wave propagates across the whole ROTE structure , enabling the volume RI sensing.

According to our previous study (Jian et al., 2010), the ROTE transmission is more sensitive to the RI change of the central slab than to that of the tunneling gaps. Therefore, the central slab is chosen as the sensing element rather than the tunneling gaps. A schematic diagram of the sensor based on ROTE is shown in Fig. 1d. In this study, K9 prisms coated with low-RI polymer layers are used to form the photonic barriers, and the cell solution injected between the two photonic barriers acts as the central slab. The polymer layer (MY-131 series, RI = 1.308 RIU, refractive index unit) forms a low-RI dielectric layer between the prism (RI = 1.59 RIU) and the liquid sample to be tested (RI = 1.35–1.37 RIU). In this way, the RI distribution has the order of high-low-high-low-high, which meets the requirement of ROTE. The detailed parameters of the sensor device are listed in Table 1. As the ROTE peak/dip of the S-polarized light is much sharper than that of P-polarized light (by a factor of 1000, Jian et al., 2010), the sensor is chosen to work in the S-polarized state in the following experiments to achieve a better performance.

Table 1 Parameters of the resonant optical tunneling effect (ROTE) multilayered structure.

Parameter	Symbol	Value
Incidence angle	α	61°
Width of tunneling gaps	d	3 μm
Width of central slab	g	300 μm
Refractive index of the input and output layers	n_{in}, n_{out}	$1.59 + 9.84\times10^{-9}\,i$
Refractive index of the tunneling gaps	n_1	$1.308 + 5\times10^{-6}\,i$
Refractive index of central slab	n_2	To be determined

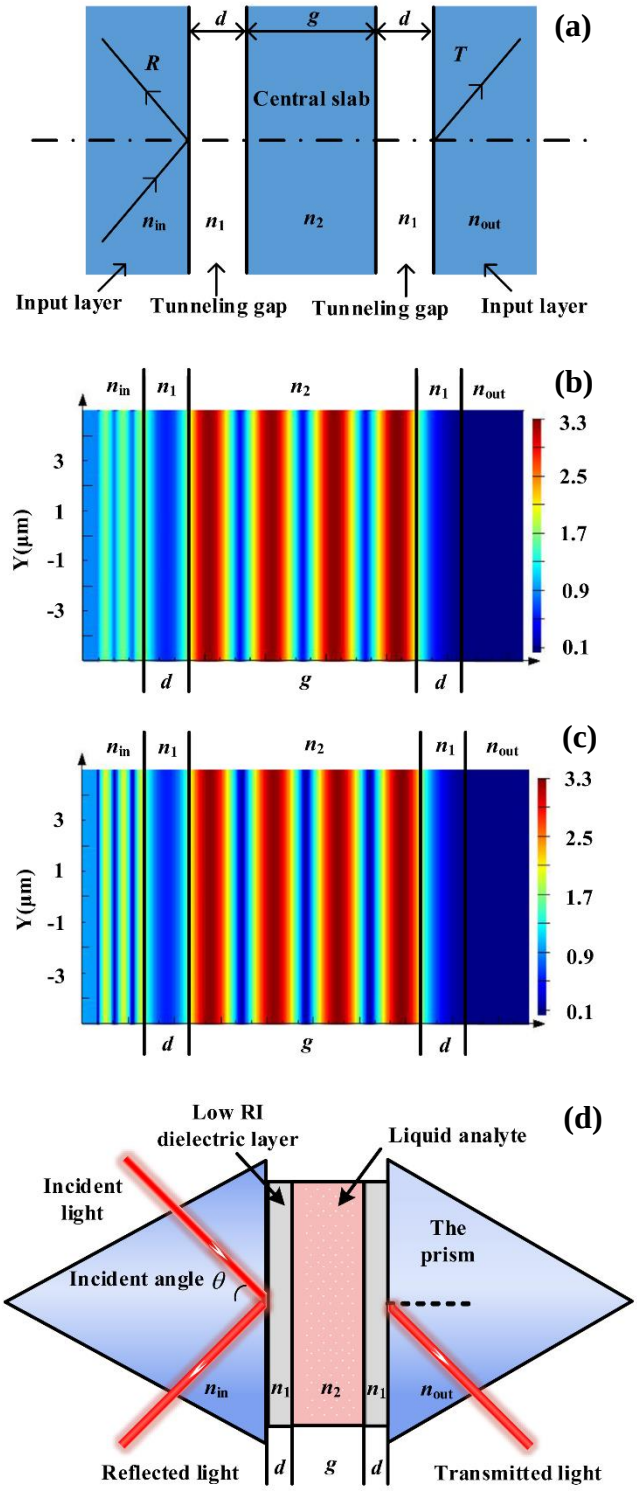

Fig. 1. (a) Schematic of the multilayer structure for the resonant optical tunneling effect (ROTE). The electric field distributions of light propagation in the ROTE structure at the resonant wavelengths of reflection for (b) the S-polarized light and (c) the P-polarized light. (d) Design of the ROTE sensor for the volume RI detection.

3. Fabrication & experimental setup

3.1 Preparation of the ROTE multilayered structure

Because the triangular prism is too heavy to be safely fixed on the spin coating machine, the low-RI polymer film cannot be directly coated on the triangular prism surface. Thus, it is coated on a glass slide with the same material (K9) of the triangular prism. Then, the glass slide is seamlessly stuck to the triangular prism reflector by a UV curing adhesive. As the thickness of the low-RI medium strongly influences the experimental results, it is carefully checked by ellipsometry before the experiment.

3.2 Experimental setup

The schematic diagram of the experimental setup is shown in Fig. 2a. Because of the low absorption of the cell in the near infrared and infrared wavelengths, a tunable infrared fiber laser (TIFL, New Focus TLB-6700) is employed as the light source to reduce the influence of the laser thermal effect on cell physiology. The polarization state of the emitted laser is tuned to be S-polarized by a fiber polarization controller (FPC) and verified by a polarization splitting prism (not shown in Fig. 2a). Before the incident laser is collimated by the fiber collimator, an optical fiber attenuator is utilized to adjust the laser intensity. In the experiment, the incident angle (61°) is greater than the total internal reflection angle by 1°. Finally, the reflected laser is collected by a photodetector (New Focus 1811-FC-AC), recorded together with the synchronous signal from the laser by a digital storage oscilloscope (DSO, GDS-2302A), and further transferred as the reflection spectrum of the ROTE structure.

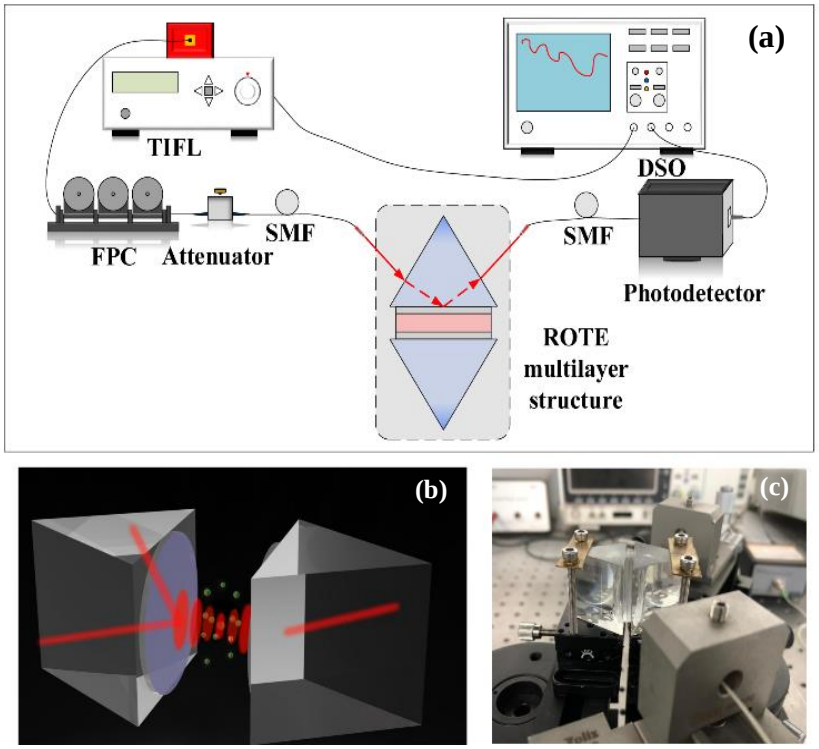

Fig. 2. Experimental setup of the ROTE sensor. (a) The whole measurement system, which utilizes an tunable infrared laser (TIFL) to sweep the wavelength range to detect the reflection spectrum; (b) Close-up and (c) photograph of the ROTE structure.

Before the test, two coated prisms are adjusted to be parallel to each other at a certain distance. Different analyte solutions are prepared to have different concentrations, whose RIs are calibrated by a commercial digital RI detector (AR200 digital hand-held refractometer). Then, one of the solutions is injected into the gap (i.e., the central slab of ROTE) between the two triangular prisms with proper pressure to overcome the surface tension. After each measurement, the gap is washed with alcohol and fully dried to restore the initial operation condition. Finally, the wavelength shift of the ROTE characteristic dip in the reflected spectrum is recorded for further analysis.

4. Results and discussion

4.1 Performance calibration using polystyrene particles

The sensor performance is first calibrated using polystyrene (PS) particles as the

same of interest before it is used to measure real cells. The PS is an optical transparent material, and the dispersed PS particles in aqueous solution are similar to the cells in culture fluid. Therefore, the PS particles are often used as a substitute for cell experiment. On the other hand, the concentrations of the PS particle solutions can be evaluated with ultrahigh accuracy by weighing the dry PS particles to be dissolved, and they are utilized to mimic the cell solution and to preliminarily characterize the performance of the ROTE sensor. In the experiment, different amounts of PS particles (5 μm diameter, standard deviation ≤ 0.027 μm, Duke Scientific Corp.) are dissolved in anhydrous ethanol as the target analyte. Because the RI of the PS particles (1.590 RIU) is larger than that of anhydrous ethanol (1.361 RIU), a higher concentration of PS particles in the mixed solution would result in a greater RI. The experimental results indicate that the ROTE absorption dip in the reflection spectrum experiences a red shift as the RI of the intermediate analyte layer increases (Fig. 3a). The sensitivity obtained is 19,000 nm/RIU, and the *Q* value of the ROTE absorption dip is 620.

As long-term laser transmission will directly heat the analyte in the central slab and change its RI during the measurement, the variation in the ROTE resonant wavelength with test time under a particular laser power is recorded (Fig. 3b). The resonant wavelength has a linear relationship with the measured time, the slope is −5 pm/min. To avoid this problem, the thermal drift is removed in all measurements in this study. A close-up of the ROTE reflection spectrum is presented in Fig. 3c to clearly show the details of the wavelength shift due to the RI variation. The experimental results coincide well with the theoretical analysis obtained by the transfer matrix method (TMM), of which more details can be found in the authors' previous work (Jian et al., 2010).

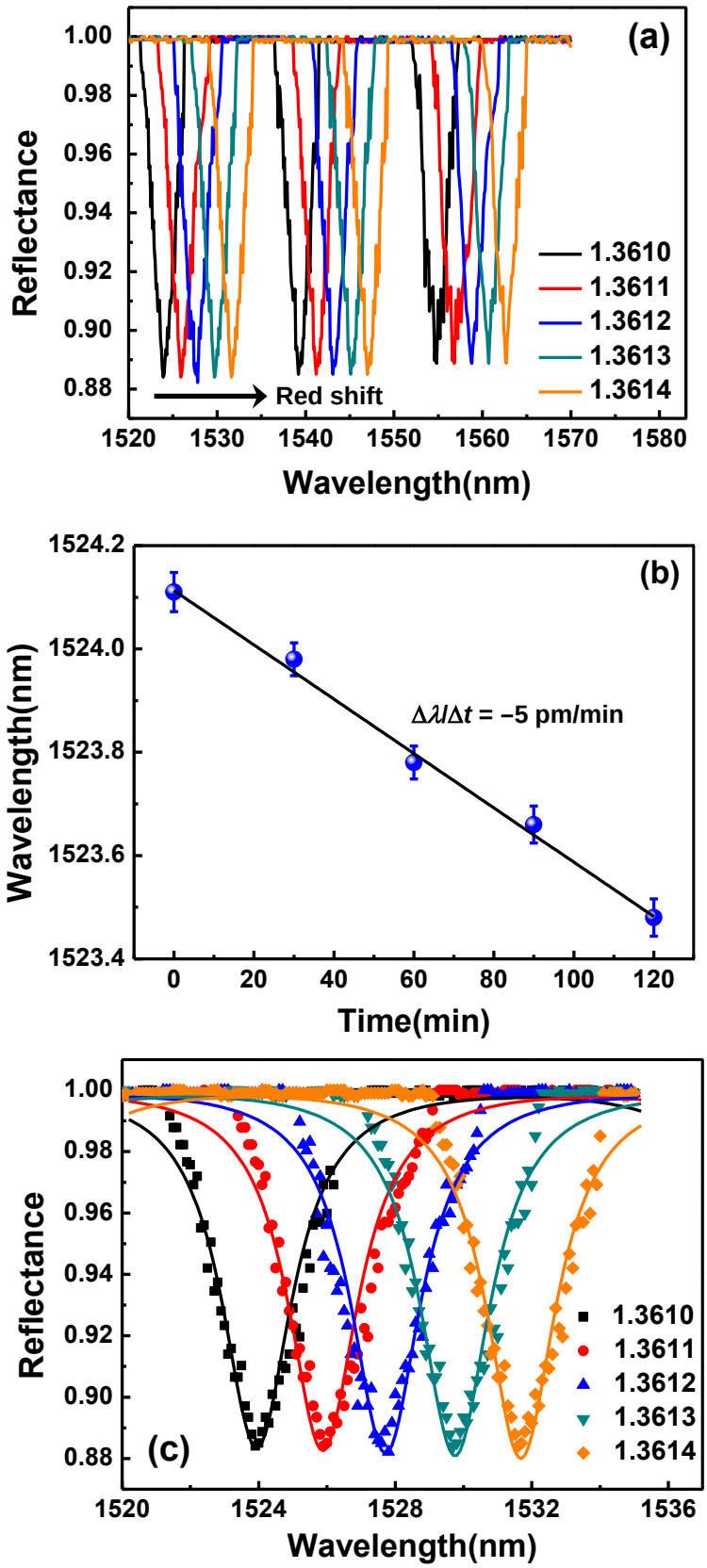

Fig. 3. (a) The shift of the resonant dip with the change of the RI of the analyte. (b) The measured thermal drift as a function of the test time. (c) Enlarged view of the resonant wavelength shift. The experimental reflection spectra are compared with the simulation results.

4.2 Q factor analysis of the ROTE dip

The experimental ROTE reflection spectrum and the simulation results are shown in Fig. 4. According to the reference (Gansch et al., 2016), the total *Q factor* of the resonator can be written as:

$$\frac{1}{Q_{total}} = \frac{1}{Q_{str}} + \frac{1}{Q_{abs}} + \frac{1}{Q_{rad}} \tag{1}$$

where Q_{rad} is the Q factor due to the coupling loss of the incident light, Q_{str} accounts for the loss of reflection and refraction in the model structure, and Q_{abs} originates from the loss of material absorption.

The values of these Q factors can be obtained from the simulation and the experiment. For instance, Q_{str} can be determined from the simulation without considering the material absorption (the red curve in Fig. 4). However, if the complex value of RI is used to take into account the material absorption (the orange curve in Fig. 4), the ROTE characteristic dip becomes significantly broader, and it gives Q_{abs} = 650 by comparing these two simulation curves. Based on the experimentally measured spectrum (the green curve in Fig. 4), it can be directly calculated to have Q_{total} = 600. Then, Q_{rad} is derived to be 1.3×10^4 by comparing the differences between the simulated and the experimental spectra.

Based on Eq. (1), the value of Q_{str} is calculated to be $Q_{str} = 1.28 \times 10^6$, which is very high. This well shows that the ROTE structure is an excellent resonator. For further comparison, the reflection spectrum of an ideal Fabry-Pérot (FP) etalon with the 99.6% reflectivity mirrors is also plotted in Fig. 4. The cavity length of the FP etalon is chosen the same as the effective length of the ROTE structure. It can be found that the FP cavity has $Q_{str} = 3 \times 10^5$, which is lower than that of the ROTE structure by one order of magnitude. Since a higher Q factor is more favorable for a higher resolution of volume sensing, the ROTE structure is used in this work to detect the cell concentration instead of the classical FP cavity.

The loss of energy is mainly due to absorption of material in the system, which includes three parts (materials), such as the prism (glass), the low-RI layer (polymer),

and the analyte solution (alcohol solution with PS particles). The main source of absorption is from the liquid analyte due to its high RI imaginary part and its large thickness (~300 μm). A dilemma arises when we try to detect a low concentration solution based on RI: higher sensitivity means a stronger light-analyte interaction, which also induces stronger absorption of the solvent (typically water or phosphate buffered solution, PBS), and thus lowered *Q* factor and reduced sensor resolution. To resolve the dilemma, we have introduced the top saturation method to greatly enhance the *Q* factor while maintaining high sensitivity and high resolution. Details will be presented below.

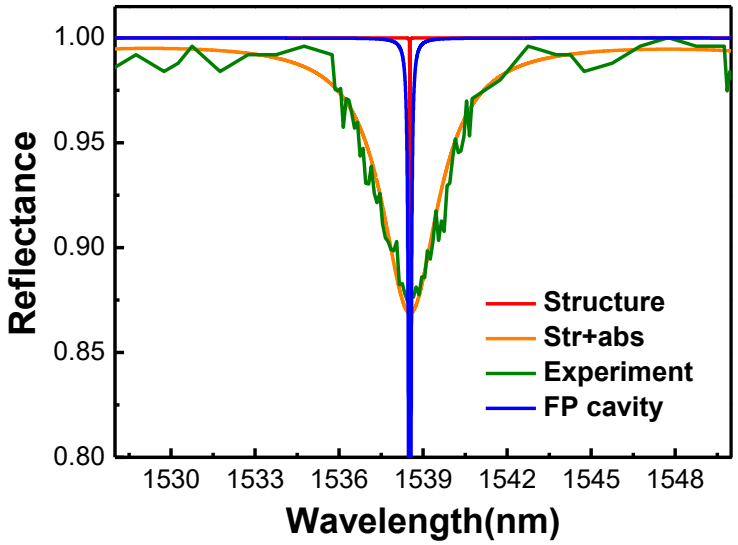

Fig. 4. Comparison of the reflection spectra of the ROTE sensor with the FP etalon. The ROTE spectra are obtained from the experiment and the simulations under different conditions (with/without absorption).

4.3 Top saturation method to enhance the Q factor

In the scanning of the reflection dips using the measurement system in Fig. 2a, it is easy to see that when the incident power is increased to the level that the detector works in the saturation state, the width of the ROTE dip would decrease dramatically. This is because only a much narrower range near the ROTE dip is not saturated while all the other parts of spectrum are saturated and become flat. This is the top saturation method. Fig. 5a presents the comparison between the ROTE absorption dip obtained

in the normal state and using the top saturation method. It is seen that the ROTE resonant dip has narrowed spectral width but at the expense of reduced depth. Our experiments find that the decreased absorption depth still allows sufficient light to transmit through and interact with the analyte liquid and PS particles/cells. The over-loaded power is limited below 8% of the saturation level of the detector (170 mW), and does not damage the photodetector according to the technical support and our own experience. By using the top saturation method, the Q factor of the ROTE dip is enhanced due to the narrowed spectral width, but the sensitivity remains unchanged since it has the same level of light-analyte interaction as that in the normal state). Therefore, the sensor resolution is improved.

In experiments, the PS particles (4.4 mg) are mixed with 1 L anhydrous ethanol to form the original solution. The solution is then diluted into five sample solutions of different concentrations. Using the PS particle data (diameter 5 μm, density 1.054 g/cm^3), the concentrations of samples are found to be c_1 =1.063 amol/ml, c_2 =2.126 amol/ml, c_3 = 3.189 amol/ml, c_4 = 4.252 amol/m, and c_5 = 5.315 amol/ml, respectively. Then, these five samples are tested in turn using the ROTE sensor, their measured reflection spectra are shown in Fig. 5b.

Figure 5(c) plots the resonant wavelength of ROTE dip as a function of the concentration of PS particles. It is seen that resonant wavelength increases linearly with higher PS particle concentration. The sensitivity of 0.18 nm/(amol/ml), corresponding to the RI sensitivity of 10^{-5} RIU. And, the sensor resolution is 1.063 amol/ml (corresponding to 6.24× 10^5 particles/ml), which will be compared with the other methods in the conclusion section below. In addition, the total Q factor of the sensor is Q_{total} = 4,000. Compared with the value Q_{total} = 600 in the normal state, the Q factor of the sensor is enhanced by about 7 times due to the use of the saturation top method. This is a special merit of this work.

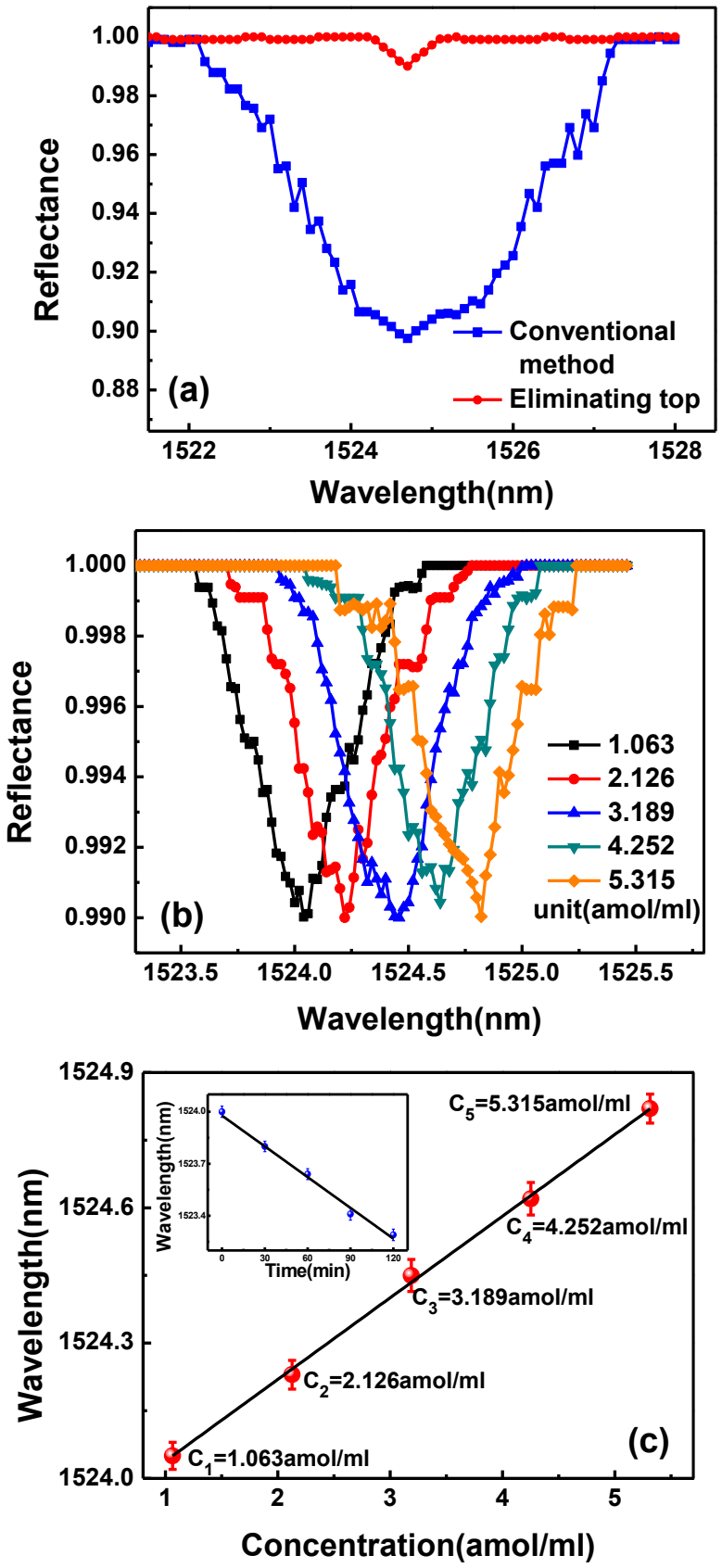

Fig. 5. (a) The ROTE dip presented in the normal state and in the top saturation method. (b) The reflection spectra in the PS particle solutions with different concentrations. (c) The variation of the

resonant wavelength with the change in PS particle concentration, the inset plots the thermal shift of the resonant wavelength with the test time.

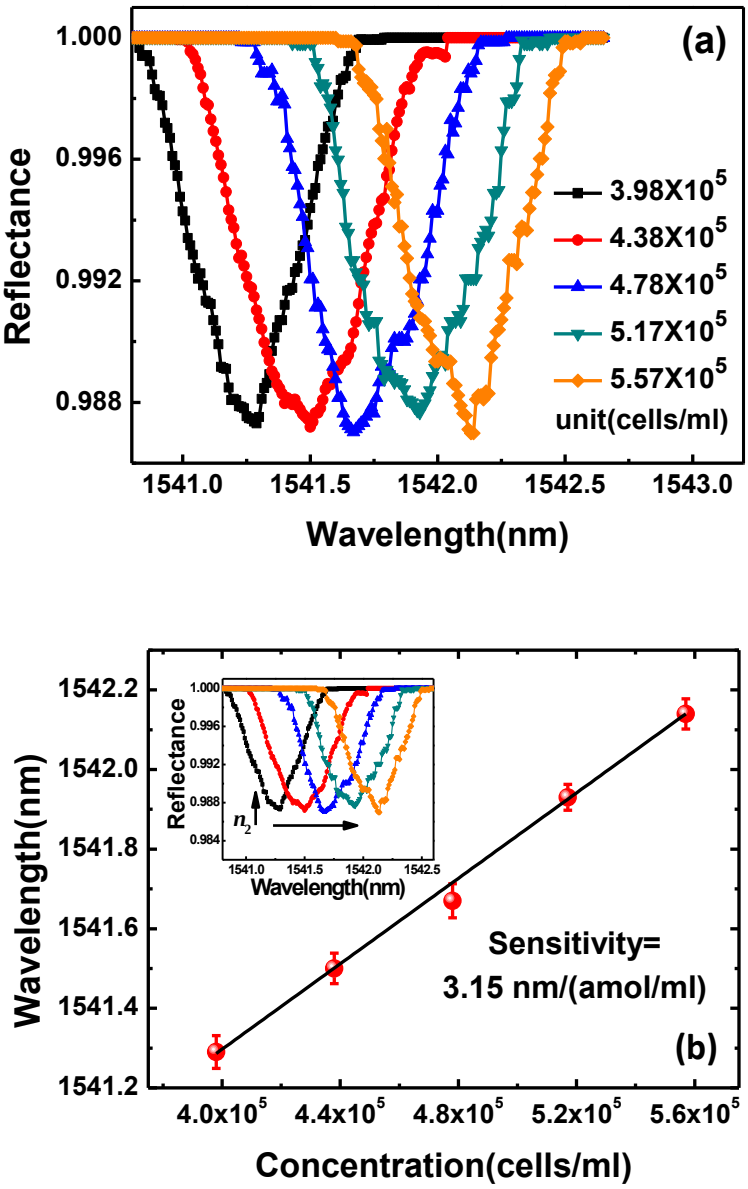

Fig. 6. (a) The ROTE dip presents a red shift as the RI of analyte increases. (b) The dependence of the ROTE resonant wavelength on the cell concentration.

4.4 Cell detection experiments

Hepatoma cells of different concentrations are used as the analyte to be measured in this experiment. The initial cell amount is counted on a hemocytometer. The pure cells are separated from the cell culture fluid by centrifugation. Then, different

amounts of cell-containing solutions (2, 2.2, 2.4, 2.6, and 2.8 μl) are extracted using a pipette before they are mixed with 500-μl RI matching solution (Cargille AA, 1.4580 RIU), which can maintain cell morphology for a certain time. Five different concentrations of cells are prepared (3.98×10^5, 4.38×10^5, 4.78×10^5, 5.17×10^5, and 5.57×10^5 cells/ml). Fig. 6a shows the ROTE reflection spectra of the five sample solutions. The RI variation can be retrieved by the shift of ROTE dip. Fig. 6b plots the dip wavelength as a function of the cell concentration. The sensitivity reaches as high as 3.15 nm/(amol/ml), and the cell concentration of 4×10^4 cells/ml can be discriminated easily (i.e., the detection limit is 4×10^4 cells/ml).

Table 2 compares our ROTE sensors with some other classical cell sensors in literature, like the localized surface plasmon resonance (LSPR) sensors [Liu et al., 2014], the Fabry–Pérot (FP) etalons [Zhu et al., 2017], the titled fiber grating (TFBG) sensors [Guo et al., 2014] and the photonic crystal fiber (PCF) sensors [Yang et al., 2015]. From Table 2, the ROTE sensor is about 40 times higher in the sensitivity and 20 times higher in the figure of merit than the state of the art. And, the detection limit of the ROTE sensor is among the best. These well demonstrates the excellent performance of our ROTE cell concentration sensor.

Table 2 Comparison of our ROTE sensor with the other classical sensors in literature, including the localized surface plasmon resonance (LSPR) sensors, the Fabry–Pérot (FP) etalons, the titled fiber grating (TFBG) sensors and the photonic crystal fiber (PCF) sensors.

Working principle	**Sensitivity (nm/RIU)**	**Q factor**	**FOM**	**Detection limit (cells/ml)**	**Reference**
LSPR	535			10^4~10^6	Liu et al., 2014
FP etalon				10^{13}	Zhu et al., 2017
LSPR + FP etalon	496			~10^4	Zhu et al., 2016
TFBG	180		2,500	~10^5	Guo et al., 2014
PCF	451	7,000	2,000		Yang et al., 2015
ROTE	**19,000**	**4,000**	**49,000**	**4×10^4**	**---**

5. Conclusions

In this study, ultra-highly sensitive cell concentration detection is experimentally demonstrated by exploiting a special physical mechanism of ROTE. By using the polystyrene particles as the model, the ROTE sensor has been calibrated to have a sensitivity of 19,000 nm/RIU and a Q value of 4,000 when the top saturation method is adopted. The experiments with hepatoma cells have shown that the detection limit of concentration resolution is as low as 4×10^4 cells/ml, which is comparable to the best results obtained by the other optical cell sensors. In addition, the ROTE sensor has the figure of merit (FOM) enhanced by one order of magnitude as compared to the state of the art. The ROTE sensor will be particularly useful for drug screening, environment protection and drinking water safety.

Acknowledgements

This study is financially supported by the National Natural Science Foundation of China (No. 61501316, 61471255, 51622507, 51505324, 81602506 and 61377068), the Shanxi Provincial Foundation for Returned Scholars (2015-047), 863 project (2015AA042601), Excellent Talents Technology Innovation Program of Shanxi Province (201605D211027), Hundreds of Talents of Shanxi Province, and Research Grants Council of Hong Kong (N_PolyU505/13, 152184/15E and 152127/17E).

References

Peltola, V., Mertsola, J., Ruuskanen, O., 2006. J. Pediatr. 149(5), 721-724.

Jarocka, U., Sawicka, R., Gora-Sochacka, A., Sirko, A., Zagorski-Ostoja, W., Radecki, J., Radecka, H., 2014. Biosens. Bioelectron. 55, 301-306.

Vaisocherova, H., Mrkvova, K., Piliarik, M., Jinoch, P., Steinbachova, M., Homola, J., 2007. Biosens. Bioelectron. 22(6), 1020-1026.

Jaitin, D.A., Keren-Shaul, H., Elefant, N., Amit, I., 2015. Semin. Immunol. 27(1), 67-71.

Fletcher, C.V., Staskus, K., Wietgrefe, S.W., Rothenberger, M., Reilly, C., Chipman, J.G., Beilman, G.J., Khoruts, A., Thorkelson, A., Schmidt, T.E., Anderson, J.,

Perkey, K., Stevenson, M., Perelson, A.S., Douek, D.C., Haase, A.T., Schacker, T.W., 2014. Proc. Natl. Acad. Sci. U.S.A. 111(6), 2307-2312.

Wallace, Z.S., Mattoo, H., Carruthers, M., Mahajan, V.S., Della Torre, E., Lee, H., Kulikova, M., Deshpande, V., Pillai, S., Stone, J.H., 2015. Ann. Rheum. Dis. 74(1), 190-195.

Guo, T., Liu, F., Liu, Y., Chen, N.K., Guan, B.O., Albert, J., 2014. Biosens. Bioelectron. 55, 452-458.

Sun, D., Guo, T., Guan, B.-O., 2017. Journal of Lightwave Technology 35(16), 3354-3359.

He, Z., Tian, F., Zhu, Y., Lavlinskaia, N., Du, H., 2011. Biosens. Bioelectron. 26(12), 4774-4778.

Rindorf, L., Bang, O., 2008. Opt Lett. 33(6), 563-565.

Hoo, Y.L., Jin, W., Xiao, L., Ju, J., Ho, H.L., 2009. Sensor. Actuat. B: Chem. 136(1), 26-31.

Wu, D.K., Kuhlmey, B.T., Eggleton, B.J., 2009. Opt. Lett. 34(3), 322-324.

Luo, Y., Chen, X., Xu, M., Chen, Z., Fan, X., 2014. Opt. Laser Technol. 56, 12-14.

Scholten, K., Fan, X., Zellers, E.T., 2014. Lab Chip 14(19), 3873-3880.

Vollmer, F., Braun, D., Libchaber, A., Khoshsima, M., Teraoka, I., Arnold, S., 2002. Appl. Phys. Lett. 80(21), 4057-4059.

Zhang, S.X., Wang, L., Li, Z.Y., Li, Y., Gong, Q., Xiao, Y.F., 2016. Opt. Lett. 41(19), 4437-4440.

Zhi, Y., Yu, X.C., Gong, Q., Yang, L., Xiao, Y.F., 2017. Adv. Mater. 29(12).

Cole, G.D., Zhang, W., Martin, M.J., Ye, J., Aspelmeyer, M., 2013. Nat. Photonics 7(8), 644-650.

Cole, G.D., Zhang, W., Bjork, B.J., Follman, D., Heu, P., Deutsch, C., Sonderhouse, L., Robinson, J., Franz, C., Alexandrovski, A., Notcutt, M., Heckl, O.H., Ye, J., Aspelmeyer, M., 2016. Optica 3(6), 647.

Hayashi, S., Kurokawa, H., Oga, H., 1999. Opt. Rev. 6(3), 204-210.

Jian, A., Zhang, X., 2013. IEEE. J. Sel. Top. Quant. 19(3), 9000310.

Yamamoto, N., Ohtani, N., 2004. Jpn. J. Appl. Phys. 43(4R), 1393.

Liu, F., Wong, M.M., Chiu, S.K., Lin, H., Ho, J.C., Pang, S.W., 2014. Biosens. Bioelectron. 55, 141-148.

Jian, A., Zhang, X., Zhu, W., Yu, M., 2010. Biomicrofluidics 4(4), 043008.

Gansch, R., Kalchmair, S., Genevet, P., Zederbauer, T., Detz, H., Andrews, A.M., Schrenk, W., Capasso, F., Lončar, M., Strasser, G., 2016. Light: Sci. Appl. 5(9), e16147.

Sherry, L.J., Chang, S.-H., Schatz, G.C., Van Duyne, R.P., Wiley, B.J., Xia, Y., 2005. Nano Lett. 5(10), 2034-2038.

Zhu, S., Li, H., Yang, M., Pang, S.W., 2016. Nanotechnology 27(29), 295101.

Zhu, J.M., Shi, Y., Zhu, X. Q., Yang, Y., Jiang, F, H., Sun, C.J., Zhao, W.H., Han, X.T., Lab Chip 17(23), 3939-4162.

Yang, D., Tian, H., Ji, Y., 2015. Photonic. Nanostruct. 15, 124-129.

Figure captions

Fig. 1. (a) Schematic of the resonant optical tunneling effect (ROTE) multilayer structure. The electric field distributions of light propagation in a ROTE structure at the resonant wavelengths for S-polarization (b) and P-polarization (c). (d) Schematic of the Sensor designed based on ROTE.

Fig. 2. (a) Schematic graph of experimental setup for the ROTE sensing system. Enlarged schematic view (b) and photograph (c) of the ROTE multilayer structure.

Fig. 3. (a) The shift of the resonant wavelength with the change of the RI of the analyte. (b) The thermal noise is quantified as test time. (c) Enlarge view of the resonant wavelength shift. The experimental reflection spectra are compared with the simulation results.

Fig. 4. Comparison of the transmission spectrum of the ROTE sensor with the transmission spectrum of the FP etalon. The ROTE spectra obtained from simulations under different assumptions (with/without absorption) also offered.

Fig. 5. (a) The ROTE dip presented in in normal state and in top saturation method (b) The reflection spectra in the PS particle solution with different concentrations. (c) The variation in resonant wavelength with the change in PS particle concentrations, the inset illustrates the effect of thermal noise/test time on the resonant wavelength.

Fig. 6. (a) The ROTE dip presents a redshift as the RI of analyte increases. (b) The cell concentrations dependence of ROTE resonant wavelength.